Branching ratio and angular distribution of ejected electrons from Eu $4f^7 6p_{1/2} nd$ auto-ionizing states*

Xiao-Rui Wu(武晓瑞)[1,2], Li Shen(沈礼)[1,2], Kai Zhang(张开)[1,2], Chang-Jian Dai(戴长建)[1,2,†], and Yu-Na Yang(杨玉娜)[1,2]

[1] *Key Laboratory of Display Materials and Photoelectric Devices, Ministry of Education, Tianjin* 300384, *China*
[2] *School of Science, Tianjin University of Technology, Tianjin* 300384, *China*

(Received 29 February 2016; revised manuscript received 24 May 2016; published online 20 July 2016)

The branching ratios of ions and the angular distributions of electrons ejected from the Eu $4f^7 6p_{1/2} nd$ auto-ionizing states are investigated with the velocity-map-imaging technique. To populate the above auto-ionizing states, the relevant bound Rydberg states have to be detected first. Two new bound Rydberg states are identified in the region between 41150 cm^{-1} and 44580 cm^{-1}, from which auto-ionization spectra of the Eu $4f^7 6p_{1/2} nd$ states are observed with isolated core excitation method. With all preparations above, the branching ratios from the above auto-ionizing states to different final ionic states and the angular distributions of electrons ejected from these processes are measured systematically. Energy dependence of branching ratios and anisotropy parameters within the auto-ionization spectra are carefully analyzed, followed by a qualitative interpretation.

Keywords: velocity-map imaging, Eu $4f^7 6p_{1/2} nd$ auto-ionizing state, branching ratio, angular distribution

PACS: 32.80.Zb, 32.30.–r, 32.80.Ee **DOI:** 10.1088/1674-1056/25/9/093203

1. Introduction

For the last decade, spectra of highly excited states of rare-earth atoms[1–3] have attracted considerable attention. Although the position and width, as well as the line shape of an auto-ionizing resonance on both Eu and Sm atoms, have been reported,[4–6] they are only relevant to total cross section of auto-ionization, yielding no information on the dynamical process of auto-ionization, such as the final states of ions, and phases of the wave function of the ejected electrons. A more stringent test of future new theory on the rare-earth atoms is to measure the branching ratios (BR) of ions and the angular distributions (AD) of electrons ejected from auto-ionizing states, as the BR may provide the information of final ionic states, while the AD represents the differential cross section of auto-ionization, providing the information about phases of possible transition channels, which is important to the physical world.[7–9]

Systematic studies of the BR and the AD on the $mp_{1/2}nd$ auto-ionizing states of alkaline-earth atoms[10,11] have been carried out previously with the time-of-flight (TOF) method,[12,13] while similar investigations on the rare-earth atoms have been reported on the Eu $4f^7 6p_{1/2} 6d$ auto-ionizing state[14,15] until recently. Although the advanced velocity-map-imaging (VMI) method,[16–18] developed originally for the photo-dissociation of molecules, was employed there, to avoid rotating the axis of the polarizer, lack of systematic studies on the $4f^7 6p_{1/2} nd$ auto-ionizing states in terms of more n values is obvious. Additionally, there will be more final ionic states involved for the higher $4f^7 6p_{1/2} nd$ auto-ionizing states with $n > 6$, more challenge has to be faced than that for the $4f^7 6p_{1/2} 6d$ state. Based on the above facts, a systematic study of the spectra, the BR, and the AD of the $4f^7 6p_{1/2} nd$ auto-ionizing states, taking $n = 7$–9 for instance, with the VMI technique is a significant task.

In Section 2 the experimental setup and methods will be presented, while the results of the BR and the AD of auto-ionization process will be discussed in Section 3. In Section 4 some conclusions will be drawn.

2. Experiment setup and methods

2.1. Experiment setup

Since the experimental apparatus used for measuring the auto-ionization BR and the AD of ejected electrons from Eu auto-ionizing states have been described in our previous work,[9] only a brief description will be given here. As shown in Fig. 1, the experimental apparatus consists of three parts: a Eu atomic beam production system, a high energy laser system, and a signal collection system.

A Eu atomic beam is produced by a resistively heated production system inside a vacuum chamber, whose pressure is kept at 10^{-5} Pa.

*Project supported by the National Natural Science Foundation of China (Grant No. 11174218).
†Corresponding author. E-mail: daicj@126.com
© 2016 Chinese Physical Society and IOP Publishing Ltd

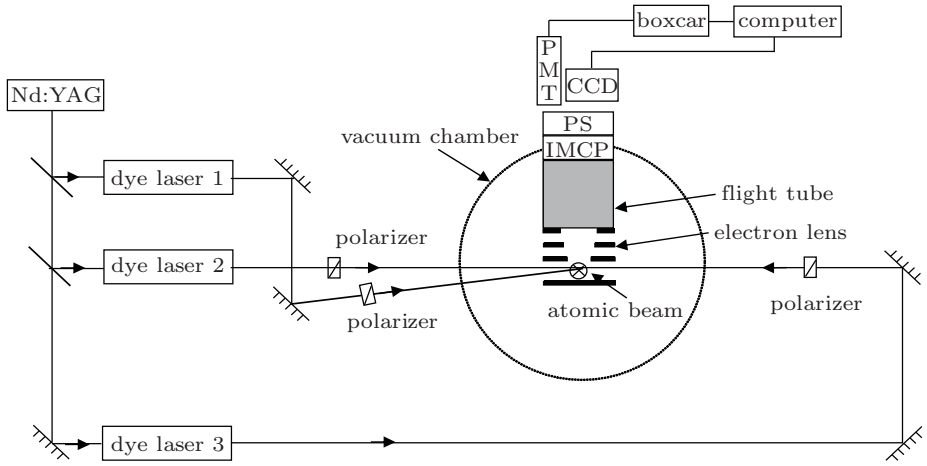


Fig. 1. Experimental setup, including an atomic beam production system, a laser system, and a signal collection system.

The three-step excitation in the experiment requires three pulsed dye lasers operated at 20 Hz, pumped by the 2nd or 3rd harmonic generation (at wavelength of 532 nm or 355 nm) of the same pulsed Nd:YAG laser. Each dye laser outputs laser pulses with a line width of 0.2 cm^{-1}, pulse width of 5–8 ns, and pulse energy of 0.5 mJ. Having passed through three linear polarizers, the three dye laser beams are propagating collinearly, and crossed with the atomic beam perpendicularly in the interaction region to avoid the Doppler broadening effect. The laser pulses of the second and the third lasers are time-delayed properly, so that the three laser pulses are sequential in time. The laser polarization directions are set with three polarizers to be perpendicular to the electric field.

The signal collection system mainly includes an electron lens,[19] a position sensitive detector (PSD), a phosphor screen (PS), and a charge coupled device (CCD). Electrons produced in the interaction region are focused by a suitable electron lens and impacted onto the PSD. The fluorescence from the PS is captured by the CCD camera and transferred to a computer for the further data analysis.

2.2. Methods

To investigate the $4f^7 6p_{1/2} nd$ auto-ionizing states, it is preferable to use the three-step isolated core excitation (ICE) method,[20] which has been utilized extensively in studies of alkaline-earth and rare-earth atoms, and has several advantages: i) only low power is required for each excitation laser; ii) the spectrum obtained by ICE is simple, where interference effects can be reduced significantly for lower-n states; iii) the n values of the $4f^7 6p_{1/2} nd$ auto-ionizing states are determined by the $4f^7 6snd$ states, which is the initial states of the third-step excitation, $4f^7 6snd \rightarrow 4f^7 6p_{1/2} nd$. However, since the $4f^7 6snd$ states have been known for $n = 6$ and 7 only,[21] one has to begin with detecting the $4f^7 6snd$ states ($n > 6$) for studying the $4f^7 6p_{1/2} nd$ ($n > 6$) auto-ionizing series.

To detect the $4f^7 6snd$ states in the region of 41150–44580 cm^{-1}, a two-color three-photon resonant ionization method[22] is employed. Furthermore, the three different paths, named Scheme I, II, and III, are designed, to uniquely determine the total angular momentum of $4f^7 6snd$ states. According to the selection rule $\Delta J = 0, \pm 1$, the possible values of angular momentum J_0 for the detected Rydberg states with Scheme I are 3/2, 5/2, or 7/2, with Scheme II are 5/2, 7/2, or 9/2, and the possible values of J_0 are 7/2, 9/2, or 11/2 with Scheme III. For example, J=9/2 can be assigned to the states that can only be detected with Scheme III.

Scheme I:

$$4f^7 6s^2 \left[{}^8S_{7/2}\right] \xrightarrow{\lambda_1} 4f^7 6s6p \left[{}^8P_{5/2}\right] \xrightarrow{\lambda_2}$$
$$[J_0 = 3/2, 5/2, 7/2] \xrightarrow{\lambda_2} Eu^+.$$

Scheme II:

$$4f^7 6s^2 \left[{}^8S_{7/2}\right] \xrightarrow{\lambda_1} 4f^7 6s6p \left[{}^8P_{7/2}\right] \xrightarrow{\lambda_2}$$
$$[J_0 = 5/2, 7/2, 9/2] \xrightarrow{\lambda_2} Eu^+.$$

Scheme III:

$$4f^7 6s^2 \left[{}^8S_{7/2}\right] \xrightarrow{\lambda_1} 4f^7 6s6p \left[{}^8P_{9/2}\right] \xrightarrow{\lambda_2}$$
$$[J_0 = 7/2, 9/2, 11/2] \xrightarrow{\lambda_2} Eu^+.$$

As illustrated above, the wavelength of the first lasers, λ_1, are fixed at 466.32 nm, 462.85 nm, and 459.53 nm to excite the Eu atom to three different $4f^7 6s6p$ states, respectively. The wavelength of the second laser, λ_2, is tuned over a certain range, to excite the Eu atom to many highly excited states, including some $4f^7 6snd$ states, which can be detected by absorbing another λ_2 photon, as shown in Fig. 2(a). Note that all wavelengths used in this paper are the values in a vacuum.

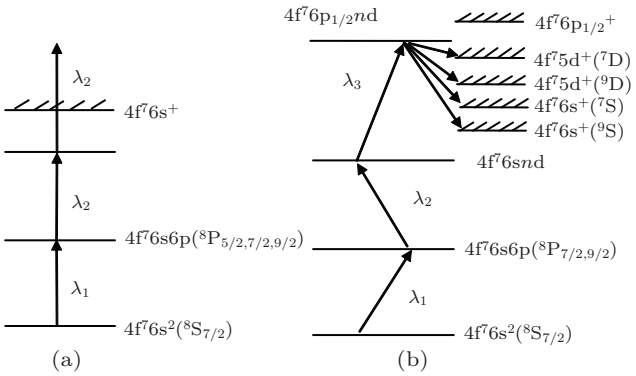


Fig. 2. The excitation schemes used in the experiment: (a) for detection of $4f^76snd$ states; (b) the ICE scheme of the $4f^76p_{1/2}nd$ states.

As shown in Fig. 2(b), once the $4f^76snd$ states are identified from the highly excited states, the $4f^76p_{1/2}nd$ auto-ionizing states can be populated with the ICE scheme. Comparisons among the spectra obtained with the above three excitation schemes can assign a unique J_0 value to any $4f^76snd$ state detected. However, there are only three highly excited states, which are shown in Table 1, that can be excited to auto-ionizing states through the ICE method.

Table 1. Values of several parameters of the three highly excited states.

Peak number	Energy/cm^{-1}	EP	J_0	δ	$4f^76snl$
1	41185.4	I, II, III	7/2	2.80	$4f^76s7d$
2	43983.6	I, II, III	7/2	2.90	$4f^76s8d$
3	44380.6	III	9/2	2.98	$4f^76s9d$

As shown in Table 1, EP represents excitation paths, δ denotes the quantum defect, and $4f^76snl$ represents electron configuration. Since δ values of $4f^76snd$ ($n = 6, 7$) states[21] are in the range of 2.79–2.90, two new electron configurations, $4f^76s8d$ and $4f^76s9d$, can be identified.

In order to obtain the total cross section of Eu $4f^76p_{1/2}nd$ series states, this work uses three different intermediate states in the ICE excitation scheme, namely,

Scheme IV:

$$4f^76s^2\left[^8S_{7/2}\right] \xrightarrow{\lambda_1} 4f^76s6p\left[^8P_{7/2}\right] \xrightarrow{\lambda_2} 4f^76s7d\left[^8D^o_{7/2}\right] \xrightarrow{\text{scan } \lambda_3} 4f^76p_{1/2}7d[J = 5/2, 7/2, 9/2].$$

Scheme V:

$$4f^76s^2\left[^8S_{7/2}\right] \xrightarrow{\lambda_1} 4f^76s6p\left[^8P_{9/2}\right] \xrightarrow{\lambda_2} 4f^76s8d\left[J = 7/2\right] \xrightarrow{\text{scan } \lambda_3} 4f^76p_{1/2}8d[J = 5/2, 7/2, 9/2].$$

Scheme VI:

$$4f^76s^2\left[^8S_{7/2}\right] \xrightarrow{\lambda_1} 4f^76s6p\left[^8P_{9/2}\right] \xrightarrow{\lambda_2} 4f^76s9d\left[J = 9/2\right] \xrightarrow{\text{scan } \lambda_3} 4f^76p_{1/2}9d[J = 7/2, 9/2, 11/2],$$

where λ_1 is fixed at 462.85 nm, 459.53 nm, and 459.53 nm, to excite the Eu atom from the ground state to different $4f^76s6p$ states, respectively. The wavelength of the second laser, λ_2, is fixed at 510.72 nm, 449.99 nm, and 442.22 nm for the Schemes IV, V, and VI, to excite the outer electron to three bound Rydberg states, respectively. Then, the third laser, whose wavelength λ_3 is scanned in a wide range depending on the situations, the auto-ionizing resonance transition from $4f^76snd$ state to $4f^76p_{1/2}nd$ state is carried out, as shown in Fig. 2(b). More interestingly, in these three excitation schemes, the Eu atom quickly decays to $4f^75d^+(^7D^o)$, $4f^75d^+(^9D^o)$, $4f^76s^+(^7S^o)$, or $4f^76s^+(^9S^o)$ ionic state with the ejection of an electron.

Electrons ejected from the process of auto-ionizing are probed by the VMI method.[16–18] Figure 3 shows an example of VMI images acquired at a point of $4f^76p_{1/2}7d$ state. Figure 3(a) displays that the two-dimensional (2D) distribution captured by the CCD is treated as the raw image, which could be reconstructed to a three-dimensional (3D) distribution of the ejected electrons by the inverted Abel transformation. Figure 3(b) shows that the 3D distribution is treated as the Abel-inverted image. The BR of ions and the ADs of electrons ejected from $4f^76p_{1/2}nd$ states can be derived by fitting the Abel-inverted images.

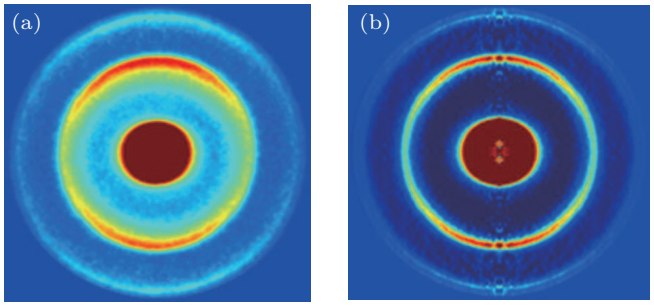


Fig. 3. (color online) The VMI images at the fixed energy of the $4f^76p_{1/2}7d$ state: the raw image (a) and the Abel-inverted image (b).

As shown in Fig. 3, there are four rings in both the raw image and the Able-inverted image, corresponding to four different ionic states shown in Fig. 2(b). Namely, the four rings from the inner to the outer denote the ADs corresponding to the decays to the $4f^75d^+(^7D^o)$, $4f^75d^+(^9D^o)$, $4f^76s^+(^7S^o)$, and $4f^76s^+(^9S^o)$ final ionic states, respectively.

In the present study, several parameters of VMI will be adjusted in order to obtain the most accurate data. To ensure that the electrons ejected from the auto-ionization are located accurately, it is necessary for the spatial location of the image with VMI to be calibrated. Namely, the ejected electrons with zero kinetic energy should be in the center of the image. In addition, the brightness calibration of the VMI image leads to

the uncertainty in boundaries within which angular integral is undertaken. In general, the uncertainty of this experiment is estimated to be 5%.

3. Results and discussion

Before describing the BR of ions and the AD of ejected electrons from $4f^7 6p_{1/2} nd$ states, the auto-ionization spectra of $4f^7 6p_{1/2} nd$ states will be discussed briefly. Eu atoms can be excited from the ground state to $4f^7 6p_{1/2} nd$ auto-ionizing states by absorbing three photons, while auto-ionization spectra of $4f^7 6p_{1/2} nd$ states are obtained by collecting the ions due to the instability of auto-ionization states.

For example, the auto-ionization spectrum (solid line) of $4f^7 6p_{1/2} 7d$ state together with the Lorentzian fitting result (dashed line) is shown in Fig. 4. The spectrum of $4f^7 6p_{1/2} 7d$ state is the standard Lorentzian profiles, indicating the success of the ICE method.

According to the above discussion, it is curious to know whether there is difference between $4f^7 6p_{1/2} 7d$ and $4f^7 6p_{1/2} nd$ ($n = 8$, 9) auto-ionizing states in terms of their spectra. As expected, the auto-ionization spectra of $4f^7 6p_{1/2} 8d$ and 9d states with the Lorentzian fitting results (dashed line) shown in Fig. 5 are also the standard Lorentzian profiles. With the assistance of Ref. [15], the three spectra of $4f^7 6p_{1/2} 6d$ auto-ionizing state are Fano-type line shapes, indicating that the ICE method is valid for Eu $4f^7 6p_{1/2} nd$ ($n \geq 7$) auto-ionizing states.

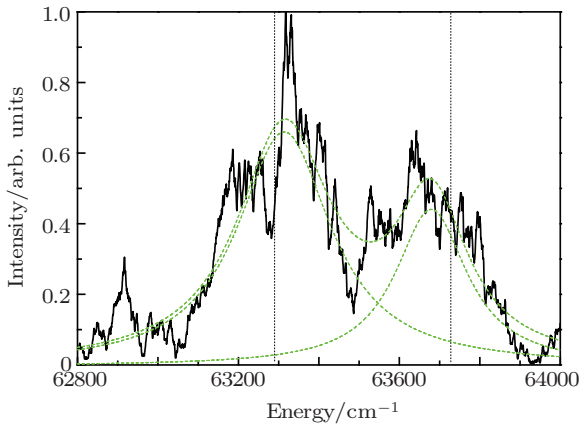


Fig. 4. (color online) Auto-ionization spectrum of $4f^7 6p_{1/2} 7d$ state in the energy range of 62800–64000 cm^{-1}.

Since λ_3 is scanned across the $4f^7 6s^+$ ($^7S^o$) $\rightarrow 4f^7 6p^+_{1/2}$ ($J = 3$) or $4f^7 6p^+_{1/2}$ ($J = 4$) ionic transition, the spectra of the auto-ionizing states with $4f^7 6p_{1/2} nd$ configuration possess double-peak profiles.

With the combination of Figs. 4 and 5, the three spectra are all superimposed with some complex structures, manifesting the interaction among different auto-ionization series converging to different ionization limits. Because the line width of the auto-ionization spectrum is inversely proportional to $(n^*)^3$, the complex structures on the top of the main profile are the auto-ionizing states converging to $4f^7 5d^+$ ionization limits, where n^* is the effective quantum number. In addition, the wide complex structures are the configuration interaction between the $4f^7 6p_{1/2} nd$ auto-ionizing states and higher-n $4f^7 5d$ (^{7}D) nl auto-ionizing states, while the narrow one converges to $4f^7 5d^+$ (^{9}D) ionization limits.

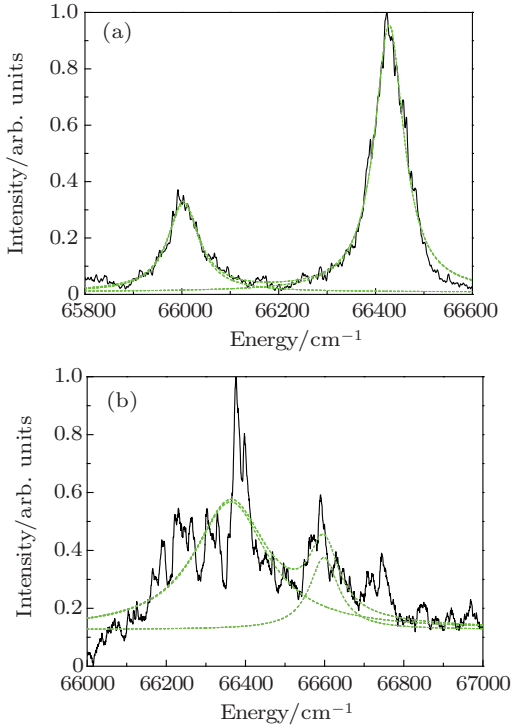


Fig. 5. (color online) Auto-ionization spectra of $4f^7 6p_{1/2} nd$ ($n = 8$, 9) auto-ionizing states: (a) the spectrum of $4f^7 6p_{1/2} 8d$ state in the energy region of 65800–66600 cm^{-1}, and (b) the spectrum of $4f^7 6p_{1/2} 9d$ state in the energy region of 66000–67000 cm^{-1}.

The energies of the three $4f^7 6p_{1/2} nd$ auto-ionizing states are different, leading to $4f^7 6p_{1/2} nd$ auto-ionizing states interacting with different $4f^7 5dnl$ states. Therefore, the three auto-ionization spectra have different complexity. Obviously, the spectrum of $4f^7 6p_{1/2} 8d$ state is the simplest one, while $4f^7 6p_{1/2} 9d$ state is the most complex.

Furthermore, the comparison between Figs. 5(a) and 5(b) shows that the line width of $4f^7 6p_{1/2} 8d$ state is smaller than those of the $4f^7 6p_{1/2} 9d$ state. This is because the line width is not only determined by the effective quantum number, but also affected by the interaction with the continuum channels.[4,14]

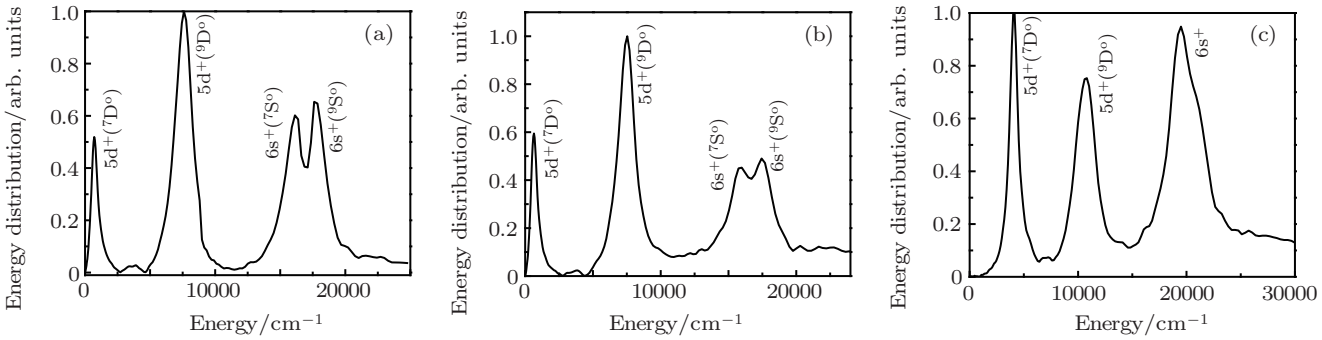


Fig. 6. Exemplified energy distributions of ejected electrons for (a) $4f^7 6p_{1/2} 7d$ state, (b) $4f^7 6p_{1/2} 8d$ state, and (c) $4f^7 6p_{1/2} 9d$ state.

Because the energy of $4f^7 6p_{1/2} 9d$ state approaches the $4f^7 6p^+_{3/2}$ ionization limit, the spectrum of $4f^7 6p_{1/2} 9d$ may also be affected by these auto-ionizing states converging to the $4f^7 6p^+_{3/2}$ ionization limit. Specifically, the spectra of $4f^7 6p_{1/2} 8d$ and 9d auto-ionizing states further confirm the existence of $4f^7 6s8d$ and $4f^7 6s9d$ bound Rydberg states.

Since the spectra of $4f^7 6p_{1/2} nd$ states provide no information about the dynamical process of auto-ionization and energy conservation results in one-to-one correspondence between the energy of the ejected electrons and the final ionic states, the energy of the ejected electrons is analyzed instead to determine the final states.

Energy distribution of ejected electrons, which can be extracted from fitting the Abel-inverted image, is a key factor in the experiment. An example is shown in Fig. 6 for the energy distribution ejected electrons from $4f^7 6p_{1/2} nd$ states.

As shown in Fig. 6(c), the fine structures of $4f^7 6s^+$ ionic state cannot be resolved, while $4f^7 6s^+ (^7S^o)$ and $4f^7 6s^+ (^9S^o)$ ionic states can be resolved in Figs. 6(a) and 6(b), indicating that with the increasing energy of ejected electrons, the resolution becomes lower. Therefore, there are four auto-ionization channels for $4f^7 6p_{1/2} 7d$ state and $4f^7 6p_{1/2} 8d$ state, respectively. There are three auto-ionization channels for $4f^7 6p_{1/2} 9d$ state.

One of the primary objectives of the present work is to discuss the BR of the $4f^7 6p_{1/2} nd$ states, which can be extracted from the energy distributions of elected electrons based on the areas under different profiles. Let BR_1, BR_2, BR_3, and BR_4 be the BRs to the four different ionic states $4f^7 6s^+ (^9S^o)$, $4f^7 6s^+ (^7S^o)$, $4f^7 5d^+ (^9D^o)$, and $4f^7 5d^+ (^7D^o)$ in Figs. 6(a) and 6(b), while BR_{12} corresponds to $4f^7 6s^+$ state in Fig. 6(c). The sum of BRs at any fixed point is equal to 1. An example is shown in Fig. 7 for the four BRs of $4f^7 6p_{1/2} 7d$ state and the auto-ionization spectrum.

As shown in Fig. 7, BR_3 is much larger than BR_1, BR_2, or BR_4, meaning that Eu atoms mainly decay to $4f^7 5d^+ (^9D^o)$ ionic state in the whole energy region. Nearly 40% of Eu atoms decay to $4f^7 5d^+ (^9D^o)$ ionic state, leading to a population inversion between $4f^7 5d^+ (^9D^o)$ and two $4f^7 6s^+$ ionic states, which is significant for developing an ion laser. Meanwhile, all peaks in the spectra of BRs in Fig. 7 seem to have no correspondence to those in auto-ionization spectrum, which can be partially attributed to the configuration interaction between the $4f^7 6p_{1/2} 7d$ auto-ionizing state and the higher-n $4f^7 5dnl$ auto-ionizing states.

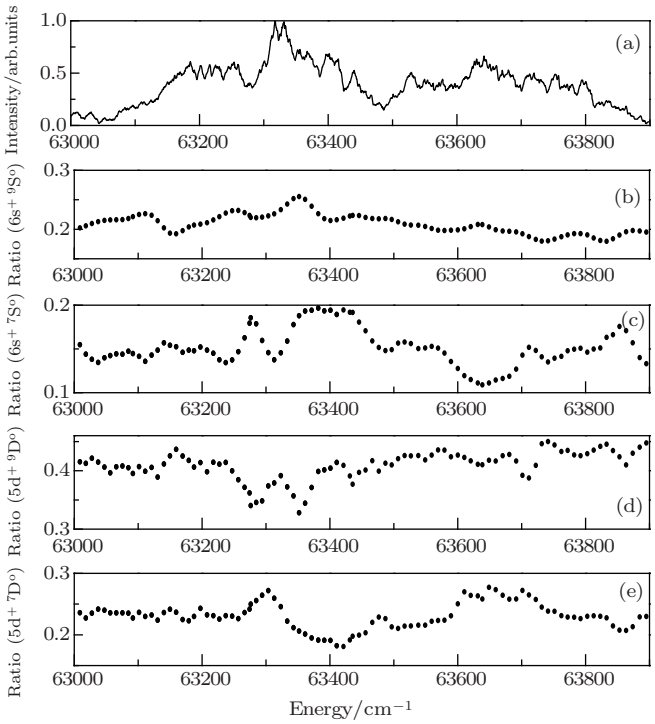


Fig. 7. The spectrum and the BRs of $4f^7 6p_{1/2} 7d$ auto-ionizing state are illustrated: (a) auto-ionization spectrum, (b) BR_1, (c) BR_2, (d) BR_3 and (e) BR_4.

Similar measurements and analysis are performed for $4f^7 6p_{1/2} 8d$ state, and the final results are presented in Fig. 8.

The population inversion between $4f^7 5d^+ (^9D^o)$ and two $4f^7 6s^+$ ionic states is still kept in the whole energy region. However, several differences between Figs. 7 and 8 can be found. For example, the BR_1, BR_2, BR_4 of the $4f^7 6p_{1/2} 8d$ state vary remarkably in the vicinity of 66000 cm^{-1}, corresponding to the auto-ionization peak on the left side.

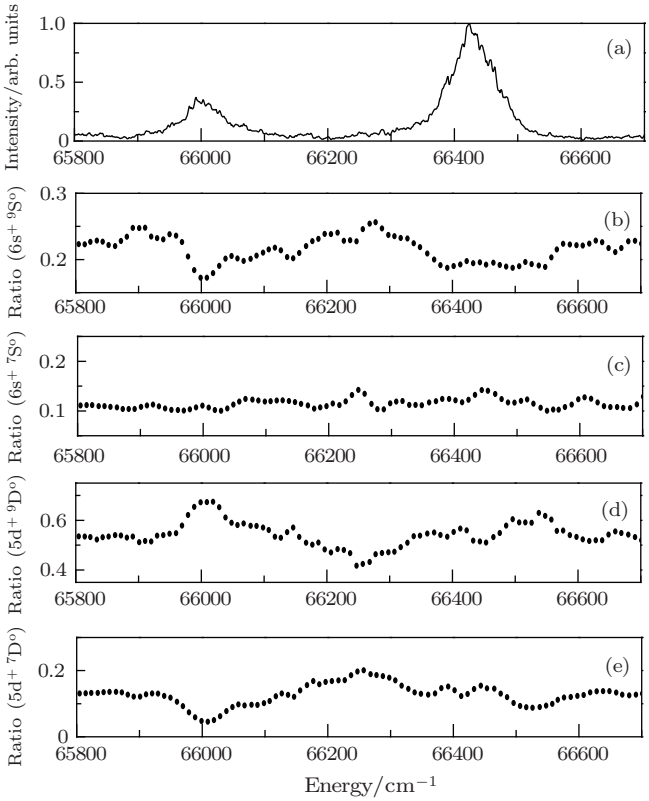


Fig. 8. The spectrum and the BRs of $4f^7 6p_{1/2}8d$ auto-ionizing state are illustrated: (a) auto-ionization spectrum, (b) BR_1, (c) BR_2, (d) BR_3, and (e) BR_4.

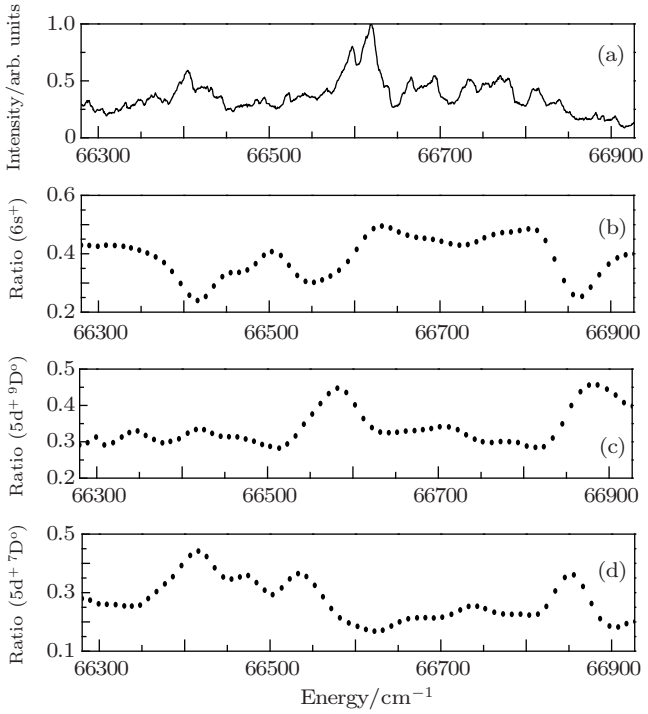


Fig. 9. The spectrum and the BRs of the $4f^7 6p_{1/2}9d$ auto-ionizing state are illustrated: (a) spectrum, (b) BR_{12}, (c) BR_3, and (d) BR_4.

The last example is shown in Fig. 9 for the auto-ionization spectrum and the BRs of $4f^7 6p_{1/2}9d$ state in a short energy region of 66300–66900 cm^{-1}, to compare with those shown in Figs. 7 and 8.

More interestingly, BR_3 is much larger than BR_{12} in the energy region of 66552.4–66917.4 cm^{-1}, and also BR_4 is much larger than BR_{12} in the energy region of 66445.1–66532.8 cm^{-1}. This means that population inversion is not only between $4f^7 5d^+(^9D^o)$ and $4f^7 6s^+$, but also between $4f^7 5d^+(^7D^o)$ and $4f^7 6s^+$ ionic state. This phenomenon can be partially attributed to the fact that the J value of $4f^7 6p_{1/2}9d$ is bigger than those of the other two auto-ionizing states. Furthermore, the BRs of the $4f^7 6p_{1/2}9d$ auto-ionizing state to the $4f^7 6s^+$, $4f^7 5d^+(^9D^o)$, and $4f^7 5d^+(^7D^o)$ ionic states fluctuate from 24% to 50%, 28% to 46%, and 16% to 44%, respectively.

After the partial cross section of $4f^7 6p_{1/2}nd$ auto-ionizing states, it is time to discuss the differential cross section. In addition, the AD of ejected electrons allows one to obtain more detailed information.

Both symmetry considerations and angular momentum selection rules constrain AD from the $4f^7 6p_{1/2}nd$ states to be of the form

$$I(\theta) = \frac{I_0}{4\pi}\sum_k \frac{\alpha_k}{\alpha_0} \mathrm{P}_k(\cos\theta) \quad (k = 0, 2, 4, 6, 8, 10, \ldots), \qquad (1)$$

where $I_0 = 4\pi\alpha_0$ is the total cross section of the auto-ionization, α_k/α_0 is the anisotropy parameter, $\mathrm{P}_k(\cos\theta)$ is the kth Legendre polynomial and k is the fitting order of the AD. Furthermore, anisotropy parameters will be determined by fitting the AD to Eq. (1) for each energy point. As mentioned in Ref. [15], two limitations of the fitting order k are $0 \le k \le 2J$ and $k = 2l_{\max}$, where l represents the orbital angular quantum. Considering the conservation of parity, we can determine that l is an odd number. Relationship of the bound Rydberg angular momentum J_0, the total angular momentum J, and the fitting order k in this paper is presented in Table 2.

Table 2. The values of fitting order in the experiment.

	$J_0 = 7/2$			$J_0 = 9/2$		
J	5/2	7/2	9/2	7/2	9/2	11/2
k	2	6	6	6	6	10

From Table 2 we can see that the highest value of k is 10. However, since the Legendre polynomials of higher orders play little role in the AD, the only anisotropy parameters up to k=6 will be displayed here. In this experiment, let $\beta = \alpha_2/\alpha_0$, $\gamma = \alpha_4/\alpha_0$, and $\varepsilon = \alpha_6/\alpha_0$, whose varying with energy is of concern in this study. An example is shown in Fig. 10.

As can be seen from Fig. 10, the anisotropy parameters β, γ, and ε fluctuate from -0.2 to 0.4, -0.2 to 0.1, and -0.1 to 0.05, respectively. The variation amplitude of the β parameter is as large again as γ and four times as large as ε, indicating that the higher orders offer some complementary contributions. In other words, the ADs of ejected electrons are well characterized by $\mathrm{P}_2(\cos\theta)$. Therefore, it is very important to discuss the anisotropy parameter β of the AD. For example, the spectra of the β parameters corresponding to

the decays to the $4f^7 6s^+(^9S^o)$, $4f^7 6s^+(^7S^o)$, $4f^7 5d^+(^9D^o)$, and $4f^7 5d^+(^7D^o)$ ionization limits together with $4f^7 6p_{1/2} 7d$ auto-ionization spectrum are shown in Fig. 11.

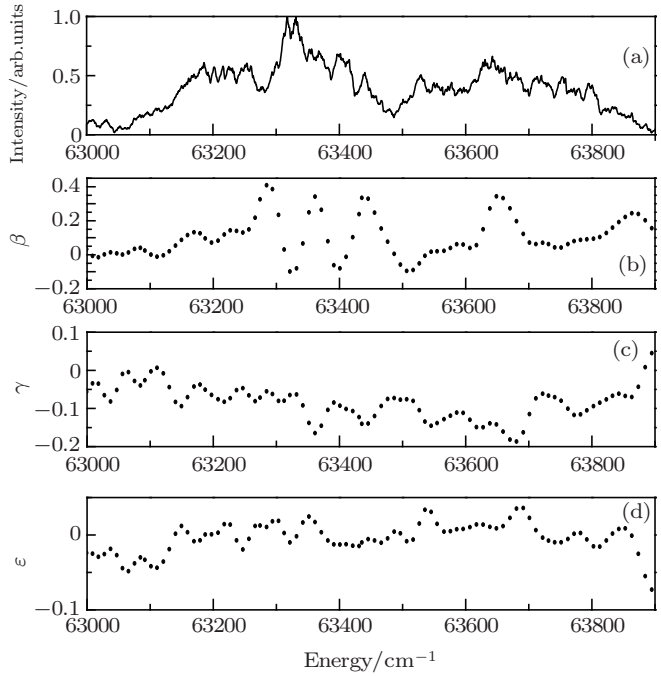


Fig. 10. Spectrum of the $4f^7 6p_{1/2} 7d$ state and spectra of the anisotropy parameters related to the $4f^7 6s^+(^9S^o)$ ionization limit. (a) Auto-ionization spectrum, (b) β, (c) γ, and (d) ε.

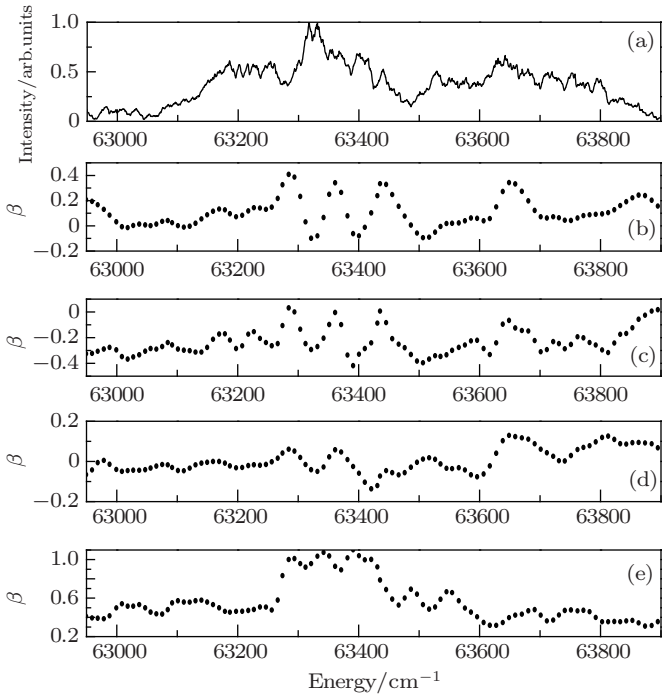


Fig. 11. Spectrum of the $4f^7 6p_{1/2} 7d$ state (a) and β spectra of $4f^7 6p_{1/2} 7d$ state related to (b) $4f^7 6s^+(^9S^o)$; (c) $4f^7 6s^+(^7S^o)$; (d) $4f^7 5d^+(^9D^o)$; (e) $4f^7 5d^+(^7D^o)$ ionization limits.

As seen from Fig. 11, some peaks in β spectra seem to correspond to the auto-ionization spectrum. For instance, in the vicinity of the left auto-ionization peak β spectra in Figs. 11(b), 11(c), and 11(e) vary remarkably, while the β spectrum in Fig. 11(d) varies in a much smaller range. This means that the ejected electron is much slower for the $4f^7 5d^+(^9D^o)$ decay than for the other three decays.

Meanwhile, the AD diagrams should be of much interest, because they reveal more intuitive space distribution of ejected electrons. AD patterns may be generated in every energy point, but only some examples will be discussed below. For example, AD patterns of electrons ejected from $4f^7 6p_{1/2} 7d$ auto-ionizing state together with auto-ionization spectrum and one β spectrum are shown in Fig. 12.

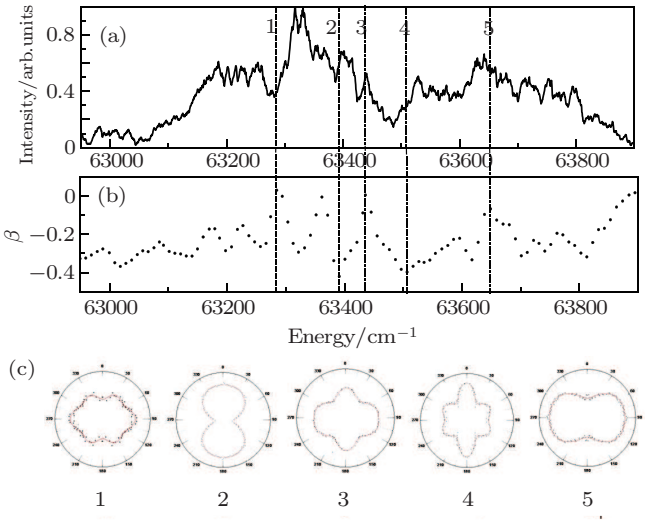


Fig. 12. (color online) Spectrum of the $4f^7 6p_{1/2} 7d$ state (a), β spectrum of $4f^7 6p_{1/2} 7d$ state related to $4f^7 6s^+(^7S^o)$ ionization limit (b), and AD patterns of $4f^7 6p_{1/2} 7d$ state related to $4f^7 6s^+(^7S^o)$ ionization limit (c).

As the three excitation lasers apply an additional force on the electron cloud in the direction of the polarization axis, the expected propensity of the AD is the electrons that are mainly ejected along the direction of the polarization axis, such as the AD patterns marked with 2 and 4. However, the unexpected patterns of the ADs marked with 1 and 5 are also discovered in Fig. 12. This means that the excitations from nd to εp and εf continuum states are accompanied by the third-step excitation. Namely, it is the 6s electron that is initially excited by the third-step laser, after which the 6pnd resonance levels decay by auto-ionization into 6sεp and 6sεf continua. Due to the complex channel interactions, the ejection of electrons at some particular energy points that are not along the polarization axis appears.

In order to make a comparison, another example for the AD patterns of $4f^7 6p_{1/2} 9d$ state is shown in Fig. 13.

What can be seen from Fig. 13 is similar to the case shown in Fig. 12, where some unexpected patterns of the AD are discovered. Some apparent differences can be seen if one examines Fig. 13 carefully. The patterns of several ADs here seem to be more complicated than those shown in Fig. 12, especially those marked by 1 and 2 in Fig. 13. On the other hand, when J value increases, a complex AD is observed.

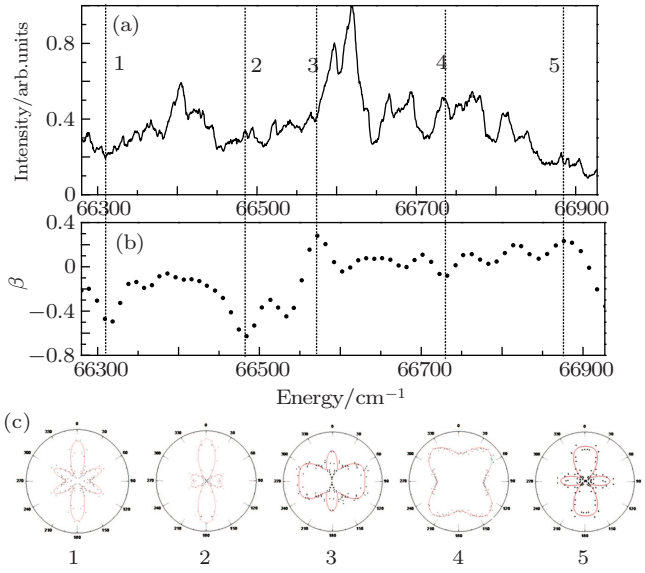


Fig. 13. (color online) (a) Spectrum of the $4f^7 6p_{1/2} 9d$ state; (b) β spectrum of $4f^7 6p_{1/2} 9d$ state related to $4f^7 6s^+$ ionization limit; and (c) AD of $4f^7 6p_{1/2} 9d$ state related to $4f^7 6s^+$ ionization limit.

As seen from Figs. 12 and 13, there is a link between the patterns of the AD and the spectrum of β parameter. Namely, the ADs are "unexpected" at some particular energies corresponding to the peak of the β spectrum, while most of the ADs are "expected" at the energies corresponding to the bottom of the β spectrum.

The last example is shown in Fig. 14 for the AD patterns of the ejected electrons from $4f^7 6p_{1/2} 8d$ state, to compare with those shown in Figs. 12 and 13.

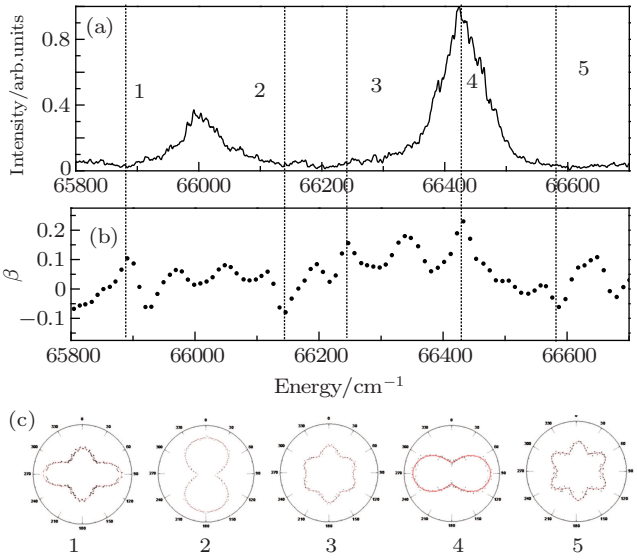


Fig. 14. (color online) (a) Spectrum of the $4f^7 6p_{1/2} 8d$ state; (b) β spectrum of $4f^7 6p_{1/2} 8d$ state related to $4f^7 5d^+ (^7S^o)$ ionization limit; and (c) AD of $4f^7 6p_{1/2} 8d$ state related to $4f^7 5d^+ (^7S^o)$ ionization limit.

The relation between the AD patterns and the spectrum of β parameter can also be seen from Fig. 14. Furthermore, what can be seen from Fig. 14 is very similar to the case shown in Fig. 12, where the AD patterns are also less complex than those shown in Fig. 13. Note that the energies of the AD patterns at the bottom of Figs. 12–14 are listed in Table 3.

Table 3. Energies marked in Figs. 12–14.

$4f^7 6s(^7S^o)7d$		$4f^7 6s(^7S^o)8d$		$4f^7 6s(^7S^o)9d$	
Peak number	Energy/cm^{-1}	Peak number	Energy/cm^{-1}	Peak number	Energy/cm^{-1}
1	63284.7	1	65890.9	1	66318.5
2	63391.3	2	66146.4	2	66484.1
3	63435.7	3	66247.2	3	66571.7
4	63503.2	4	66433.1	4	66727.2
5	63649.0	5	66587.1	5	66876.5

A comparison of Figs. 12–14 shows that the patterns of the AD correspond to the feature of the auto-ionization spectrum at some energy points. Namely, the patterns of the AD are more complex in the off-peak region of the auto-ionizing spectrum than those in the peak region. For example, those marked by 5 in Fig. 14 and marked by 3, 5 in Fig. 13 are much more diverse than those marked by 4 in Figs. 13 and 14. It is quite remarkable that the AD of electrons exhibits such dramatic variations across an auto-ionization resonance. The only logical explanation is that the Rydberg–continuum coupling is weaker at the peak than at other positions.[15] Namely, in the peak positions, the higher probability of auto-ionization may lead to weaker Rydberg–continuum coupling, thereby gaining simple patterns of the AD.

4. Conclusions

A detailed study of the auto-ionization dynamics of Eu atom, which consists of the auto-ionization spectra, the BRs of ions, and the ADs of ejected electrons, is undertaken. From the systematical study of the auto-ionization spectra of multiple d states, it is found that the ICE method is valid for the higher-n 6pnl auto-ionizing state of the Eu. Both the auto-ionization spectra and the BRs of the $4f^7 6p_{1/2} nd$ auto-ionizing states reveal the complex configuration interaction between $4f^7 6p_{1/2} nd$ auto-ionizing states and the $4f^7 5dnl$ auto-ionizing series. The link between AD patterns and the β spectrum is a significant finding from the systematic study, indicating that the AD patterns are not only influenced by the Rydberg–continuum coupling but also by the complex channel interac-

tions.

On the whole, $4f^7 6p_{1/2} 9d$ auto-ionizing state is a particular state that belongs to $4f^7 6p_{1/2} nd$, but it is the different $4f^7 6p_{1/2} 7d$ state and $4f^7 6p_{1/2} 8d$ state in case of the auto-ionizing spectrum, the auto-ionization BRs and the ADs of ejected electrons. Furthermore, in view of the specificity of $4f^7 6p_{1/2} 9d$ state, $4f^7 6p_{3/2} nl$ auto-ionizing series states need to be investigated further.

References

[1] Zhang J, Shen L and Dai C J 2015 *Chin. Phys. B* **24** 113201
[2] Yang J H, Wang X, Shen L and Dai C J 2013 *Acta Optica Sin.* **33** 1030002 (in Chinese)
[3] Xie J, Dai C J and Li M 2011 *J. Phys. B: At. Mol. Opt. Phys.* **44** 015002
[4] Wang X, Shen L and Dai C J 2012 *J. Phys. B: At. Mol. Opt. Phys.* **45** 165001
[5] Li M, Dai C J and Xie J 2011 *J. Quantative Spectroscopy Radiative Transfer* **112** 793
[6] Jing H, Ye S W and Dai C J 2015 *Chin. Phys. B* **24** 013203
[7] Kachru R, Tran N H, Pillet P and Gallagher T F 1985 *Phys. Rev. A* **31** 218
[8] Dong C, Shen L, Yang J H and Dai C J 2014 *Acta. Optica Sin.* **34** 0702001 (in Chinese)
[9] Liang H R, Shen L, Jing H and Dai C J 2014 *Acta Phys. Sin.* **63** 133202 (in Chinese)
[10] Dai C J 1996 *Phys. Rev. A* **53** 3237
[11] Lü J, Dai C J, Xu Y F and Li S B 2001 *Chin. Phys. Lett.* **18** 516
[12] Lindsay M D, Cai L T, Schinn G W, Dai C J and Gallagher T F 1992 *Phys. Rev. A* **45** 231
[13] Lindsay M D, Dai C J, Cai L T, Gallagher T F, Robicheaux F and Gteene C H 1992 *Phys. Rev. A* **46** 3789
[14] Yan J G, Shen L, Liang H R and Dai C J 2015 *Chin. Phys. B* **24** 083203
[15] Zhang K, Shen L, Dong C and Dai C J 2015 *Chin. Phys. B* **24** 103204
[16] Ashfold M N R, Nahler H N, Orr-Ewing A J, *et al.* 2006 *Phys. Chem. Chem. Phys.* **8** 26
[17] Stodolna A S, Rouzee A, Lepine F, Cohen S, Robicheaux F, Gijsbertsen A, Jungmann J H, Bordas C and Vrakking M J J 2013 *Phys. Rev. Lett.* **110** 213001
[18] Tauro S and Liu K 2008 *J. Phys. B: At. Mol. Opt. Phys.* **41** 225001
[19] Eppink A T J B and Parker D H 1997 *Rev. Sci. Instrum.* **68** 3477
[20] Dai C J, Schinn G W and Gallagher T F 1990 *Phys. Rev. A* **42** 223
[21] Martin W C, Zalubas R and Hagan L 1978 *Energy Levels-The Rare Earth Elements* (Washington: National Bureau of Standards) pp. 185–198
[22] Xie J, Dai C J and Li M 2010 *Acta Optica Sin.* **30** 2142 (in Chinese)